

Engineering altermagnetic symmetry to enable anomalous Hall response in $\text{Cr}_{1-x}\text{Mn}_x\text{Sb}$

Miriam G. Fischer^{†,1} Lukas Odenbreit^{†,1} Olena Gomonay^{†,1} Jairo Sinova,¹ Thibaud Denneulin,² Joseph V. Vaz,² Rafal E. Dunin-Borkowski,² Tommy Kotte,³ Toni Helm,³ Mathias Kläui,¹ and Martin Jourdan¹

¹*Institut für Physik, Johannes Gutenberg-Universität, Staudinger Weg 7, 55128 Mainz, Germany*

²*Ernst Ruska-Centre for Microscopy and Spectroscopy with Electrons,*

Forschungszentrum Jülich, 52425, Jülich, Germany

³*Hochfeld-Magnetlabor Dresden, Helmholtz-Zentrum Dresden-Rossendorf,
Bautzener Landstrasse 400, 01328 Dresden, Germany*

Altermagnets are a promising class of materials for spintronic applications. However, compounds that simultaneously combine the symmetry required to support an anomalous Hall effect with good metallic conductivity and magnetic ordering temperatures well above room temperature remain elusive. Here, we demonstrate that partial substitution of Cr by Mn in epitaxial CrSb(100) thin films provides a viable route to engineer the combined structural and magnetic symmetry necessary to enable an otherwise symmetry-forbidden anomalous Hall effect. By systematically exploring the magnetic phase diagram of $\text{Cr}_{1-x}\text{Mn}_x\text{Sb}$ thin films, we identify a pronounced anomalous Hall effect in $\text{Cr}_{0.75}\text{Mn}_{0.25}\text{Sb}$. Guided by Landau theory, we model the field-driven reorientation of the Néel vector and the resulting anomalous Hall response, achieving good qualitative agreement with the experimental observations.

* email: Jourdan@uni-mainz.de

[†] These authors contributed equally to this work.

INTRODUCTION

Altermagnets are promising for spintronics due to their potential to combine key advantages of both conventional antiferromagnets—such as ultrafast spin dynamics—and ferromagnets, namely, the ability to generate spin-polarized currents. Altermagnetism arises from the interplay between a specific crystal symmetry and a compensated collinear arrangement of identical magnetic moments. To realize altermagnetism, the lattice sites of two ferromagnetically ordered sublattices—whose moments are aligned antiparallel to each other—must be related by a combined translational and rotational symmetry operation. This symmetry leads to a direction-dependent exchange interaction, manifesting as an alternating spin splitting of the electronic bands [1–5]. Furthermore, despite zero net magnetization, an anomalous Hall-effect (AHE) enabling the read-out of the direction of the Néel vector can occur [1]. In contrast to the altermagnetic splitting of the electronic bands, this effect requires spin-orbit coupling. The AHE always appears together with weak ferromagnetic behaviour, i. e. canted spin moments due to a Dzyaloshinsky-Moriya type interaction [6], as they share the same symmetry based requirements to exist [7].

The most compelling experimental evidence for altermagnetic band splitting has been provided by angle-resolved photoemission spectroscopy (ARPES) studies of the isostructural intermetallic compounds MnTe [9–11] and CrSb [12, 13], classified as g-wave altermagnets due to their hexagonal symmetry. The magnetically ordered

state of both compounds consists of ferromagnetic (001) planes, which are coupled antiferromagnetically along the c-axis. However, in MnTe, the Néel vector lies within the hexagonal c-plane and aligns along the [1100] crystallographic direction enabling an AHE [7]. In contrast, in CrSb the Néel vector points along the crystallographic c-axis [19], a direction that does not provide the magnetic-space symmetry required for an AHE [14].

This is disadvantageous for potential spintronics applications, as otherwise CrSb stands out due to its relatively high magnetic ordering temperature of 700 K [16] and its metallic band structure with a significant altermagnetic spin splitting ($\simeq 0.6$ eV) positioned just below the Fermi energy [12]. Thus, a proper combination of the magnetic and electronic properties of CrSb and MnTe would result in a very promising altermagnet.

Here, we demonstrate that partial substitution of Cr with Mn in the parent compound CrSb enables tuning of the magnetocrystalline anisotropy and engineers the symmetry and magnetic order to allow for an AHE signal. For the composition $\text{Cr}_{0.75}\text{Mn}_{0.25}\text{Sb}$, we observe an AHE in (100)-oriented epitaxial thin films, which is fully consistent with the expected altermagnetic properties associated with the magnetic space symmetry of this specific sample composition. We explain the origin of the magnetic field dependence of the AHE and its relation to the orientation of the Néel vector by a Landau-type phenomenological model based on symmetry considerations.

RESULTS AND DISCUSSION

Sampling the magnetic phase diagram of $\text{Cr}_{1-x}\text{Mn}_x\text{Sb}$

Motivated by an early report of a complex magnetic

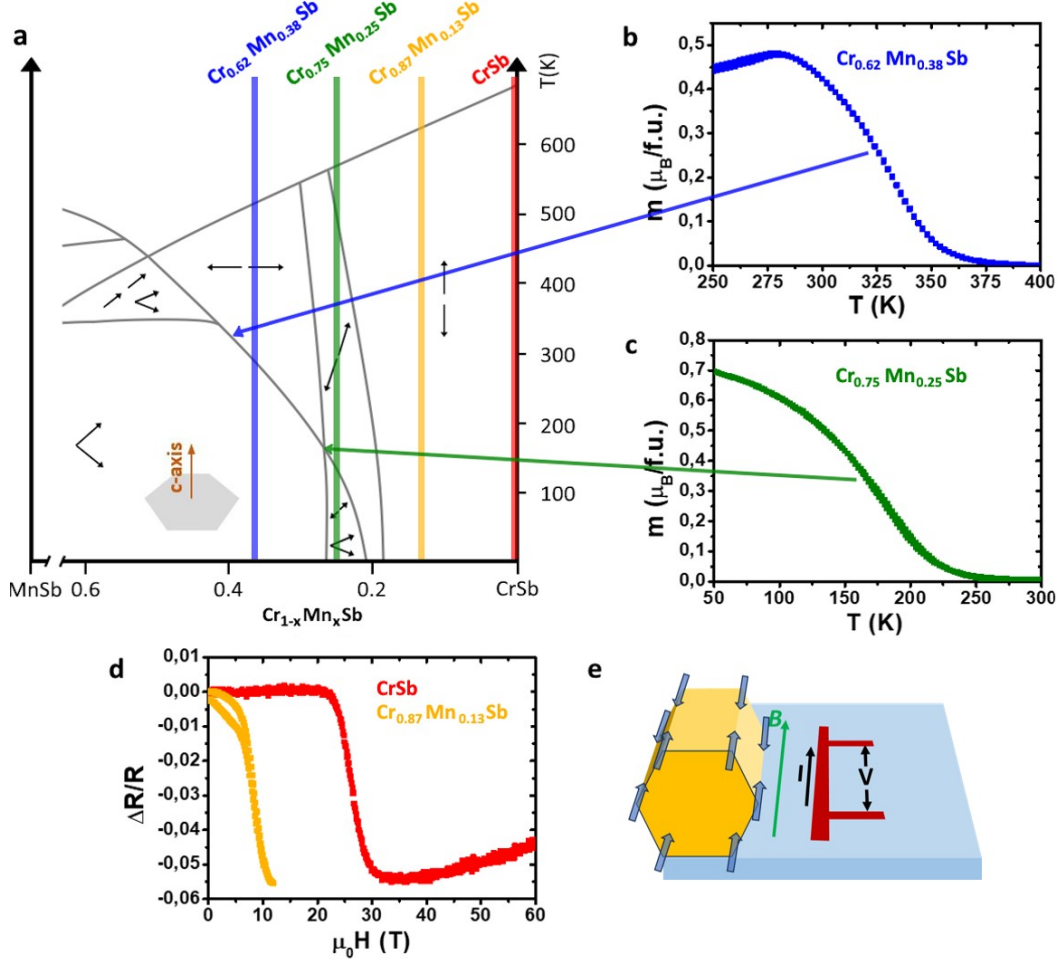


FIG. 1. Magnetic orientation of $\text{Cr}_{1-x}\text{Mn}_x\text{Sb}$ samples. **a** Magnetic phase diagram of $\text{Cr}_{1-x}\text{Mn}_x\text{Sb}$. The arrows represent the direction of the magnetic moments, where upwards and downwards align with the crystallographic c-axis and left and right correspond towards ab-plane. **b** Temperature-dependant phase transition of $\text{Cr}_{0.62}\text{Mn}_{0.38}\text{Sb}$. **c** Temperature-dependant phase transition of $\text{Cr}_{0.75}\text{Mn}_{0.25}\text{Sb}$. **d** Spin-flop transition of CrSb (red) and $\text{Cr}_{0.87}\text{Mn}_{0.13}\text{Sb}$. **e** CrSb and $\text{Cr}_{0.87}\text{Mn}_{0.13}\text{Sb}$ sample orientation during the spin-flop transition measurement.

phase diagram in bulk $\text{Cr}_{1-x}\text{Mn}_x\text{Sb}$ samples [17], we have grown corresponding (1000)-oriented epitaxial thin films on $\text{GaAs}(110)$ substrates by DC sputtering (see *Methods* and Supplementary Information). By varying the Cr-to-Mn ratio, we obtain distinct magnetic phases, whose accurate identification is essential in the context of altermagnetism. This identification is achieved through comparison with the magnetic phase diagram reported in Ref. [17], which is based neutron diffraction studies of bulk single crystals.

In Fig. 1, we classify the epitaxial thin film samples within the magnetic phase diagram based on their composition, ferromagnetic transition temperature, and magnetic anisotropy. Panel a shows the relevant region of the phase diagram with the compositions of three epitaxial $\text{Cr}_{1-x}\text{Mn}_x\text{Sb}(100)$ thin films as determined by energy dispersive X-ray spectroscopy (EDX) performed in a transmission electron microscope (TEM). Panels b and c

display temperature dependent magnetization measurements of the $\text{Cr}_{0.62}\text{Mn}_{0.38}\text{Sb}$ and $\text{Cr}_{0.75}\text{Mn}_{0.25}\text{Sb}$ films, respectively, aquired in a magnetic field of 200 mT. Both curves exhibit a transition from compensated order to a ferromagnetic state at temperatures consistent with the phase diagram shown in panel a. In contrast, and again in agreement with the phase diagram, such a transition is absent for $\text{Cr}_{0.87}\text{Mn}_{0.13}\text{Sb}$, which is expected to exhibit the same easy c-axis magnetic order as the parent compound CrSb , albeit with a reduced magnetocrystalline anisotropy energy. This reduction is confirmed by measurements of the spin-flop field, identified by an abrupt change of the sample resistance. As shown in panel d, the spin flop field of $\text{Cr}_{0.87}\text{Mn}_{0.13}\text{Sb}$, measured in the geometry illustrated in panel e, is reduced compared to that of CrSb (see Supplementary Information for a quantitative analysis).

The excellent agreement between the magnetic prop-

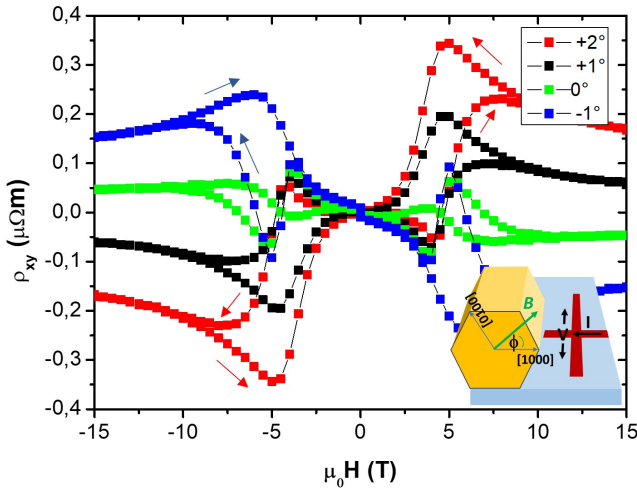


FIG. 2. **Hall-resistivity of $\text{Cr}_{0.75}\text{Mn}_{0.25}\text{Sb}(100)$.** Magnetic field dependence of the Hall-resistivity at 300 K for field directions close to the in-plane [1000]-direction. The inset shows a schematic representation of the sample geometry indicating the angle ϕ by which the magnetic field direction is tilted with respect to the in-plane [1000]-direction.

erties of the four epitaxial thin-film compositions investigated here and the magnetic phase diagram (panel **a**) of $\text{Cr}_{1-x}\text{Mn}_x\text{Sb}$ single crystals provides strong evidence that the magnetic structure of the thin films is in line with expectations from the bulk samples.

Anomalous Hall-effect in $\text{Cr}_{0.75}\text{Mn}_{0.25}\text{Sb}(100)$
 We focus on the composition $\text{Cr}_{0.75}\text{Mn}_{0.25}\text{Sb}$ because its magnetic ordering, characterized by a generic orientation of the Néel vector, allows for an anomalous Hall response within the (100)-orientated thin film geometry, as discussed in detail below. In epitaxial $\text{Cr}_{0.75}\text{Mn}_{0.25}\text{Sb}(100)$ thin films at 300 K, we observe a strongly nonlinear Hall response featuring two hysteresis loops, which we attribute to the AHE. Figure 2 shows a pronounced increase in the Hall voltage within the magnetic-field range of 3–5 T when the field direction is slightly tilted away from the in-plane [1000] direction of the sample; the measurement geometry is illustrated in the inset.

Notably, none of the other $\text{Cr}_{1-x}\text{Mn}_x\text{Sb}$ compositions shown in Fig. 1 exhibit comparable behavior, although a strain-induced AHE has recently been reported for epitaxial $\text{CrSb}(100)$ thin films [14]. Contributions from ferromagnetic impurities to our Hall signal can be excluded on the basis of field dependent magnetization measurements (see Supplementary Information).

The hysteretic nonlinearity observed in the Hall effect of our $\text{Cr}_{0.75}\text{Mn}_{0.25}\text{Sb}(100)$ thin films therefore indicates that a magnetic field $\mu_0\mathbf{H}$ in the range of 3–5 T, applied at a specific orientation, allows us to align the Néel vector \mathbf{n} into a configuration that enables the observation of an AHE.

To characterize the magnetic anisotropy, which is es-

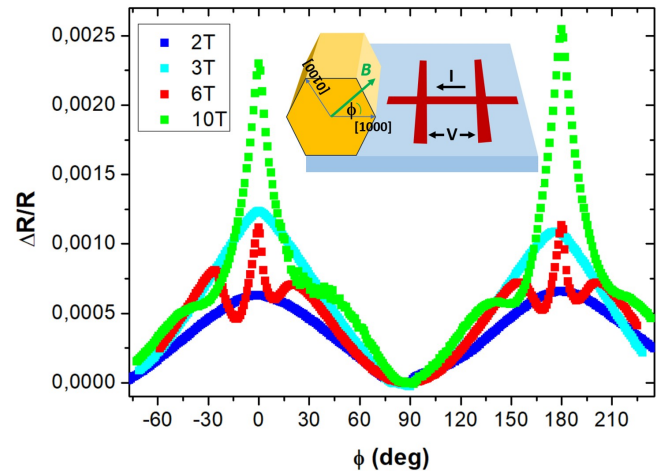


FIG. 3. **Longitudinal magnetoresistance (AMR) of $\text{Cr}_{0.75}\text{Mn}_{0.25}\text{Sb}(100)$.** Dependence of the longitudinal resistance on the orientation of magnetic fields with different magnitude (at 300 K). The inset shows a schematic representation of the sample geometry indicating the angle ϕ by which the magnetic field direction is tilted with respect to the in-plane [1000]-direction.

sential for modeling the magnetic field driven motion of the Néel vector, we use angular dependent measurements of the longitudinal anisotropic magnetoresistance (AMR).

Longitudinal anisotropic magnetoresistance of $\text{Cr}_{0.75}\text{Mn}_{0.25}\text{Sb}(100)$

Within the hexagonal c-plane, the magnetocrystalline anisotropy is generally weak so that even moderately strong magnetic fields can reorient the c-plane component of the Néel vector. Assuming perfect hexagonal symmetry, a magnetic field rotating by an angle ϕ around the c-axis of $\text{Cr}_{0.75}\text{Mn}_{0.25}\text{Sb}(100)$ would therefore reflect this weak six-fold symmetry and induce a corresponding smooth rotation of the Néel vector. However, we observe a two-fold rotational symmetry of the longitudinal resistance $R_{\text{AMR}}(\phi)$, as shown in Fig. 3. This symmetry can be explained by uniaxial strain within the film plane, which is originating from the epitaxial growth on $\text{GaAs}(110)$, i.e., on a substrate cut with a two-fold in-plane symmetry.

At sufficiently large magnetic fields (> 5 T), the angular dependence of the AMR $R_{\text{AMR}}(\phi)$, exhibits a pronounced and sharp peak at $\phi = 0^\circ$. This peak indicates that, within the c-plane, the [1000] direction is energetically favored, allowing us to infer that, in zero field, the Néel vector lies within the film plane. When a sufficiently strong magnetic field is applied along the [1000] direction, it induces a rotation of the Néel vector into a state with an out-of-plane component—analogous to a spin-flop transition—thereby modifying the AMR.

With this insight, we are able to model the field-driven

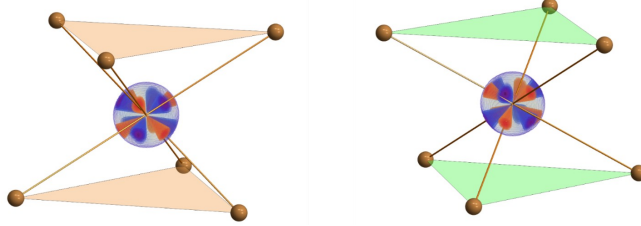


FIG. 4. **Altermagnetic order parameter.** Schematic representation of the two altermagnetic sublattices with the Cr atom in the center and the surrounding Sb atoms. The red and blue lobes represent the spherical harmonics whose difference represents the altermagnetic order parameter.

reorientation of the Néel vector and its impact on the Hall response, which is essential to unambiguously attribute the observed nonlinear Hall signal to an intrinsic AHE arising from the altermagnetic nature of the system.

Modeling Néel vector orientation, AHE and AMR of $\text{Cr}_{0.75}\text{Mn}_{0.25}\text{Sb}(100)$

Our micromagnetic modeling of the dynamics of the Néel vector $\mathbf{n} = \mathbf{M}_1 - \mathbf{M}_2$ and the total magnetization $\mathbf{m} = \mathbf{M}_1 + \mathbf{M}_2$ is guided by Landau's theory of magnetic phase transitions. Within this framework, the free energy is expressed as a power-series expansion in a generalized order parameter, constrained by the symmetries of the system. For a conventional antiferromagnet, this order parameter is simply the Néel vector. In contrast, collinear altermagnetism arises from the symmetry of the non-magnetic atomic environment surrounding the magnetic sublattices, such that mapping one sublattice onto the other requires a combined partial translation within the unit cell and a rotation. Consequently, an adequate altermagnetic order parameter must be used to capture this local symmetry [21]. We employ spherical harmonics to represent the orientation of the electronic bonds associated with each magnetic sublattice. The red and blue lobes shown in Fig. 4 indicate positive and negative weights of these bonds, respectively, thereby defining an anisotropy profile for the Néel vector \mathbf{n} and the magnetization \mathbf{m} . The altermagnetic order parameter Q_{AM} is then defined as the difference between the corresponding spherical harmonics (see Supplementary Information).

We derive the equilibrium orientations of \mathbf{n} and \mathbf{m} by minimizing the free-energy functional of $\text{Cr}_{1-x}\text{Mn}_x\text{Sb}$ in the presence of an external magnetic field \mathbf{H} . As detailed in the Supplementary Information, the free energy includes an exchange term that enforces antiparallel alignment of the sublattice magnetizations \mathbf{M}_1 and \mathbf{M}_2 , as well as a Zeeman term that aligns \mathbf{m} parallel to \mathbf{H} . In addition, Dzyaloshinskii–Moriya interactions (DMI) arise from a combination of the exchange and local anisotropy fields of the parent hexagonal lattice, and from symmetry breaking induced by growth-related strain within the film plane.

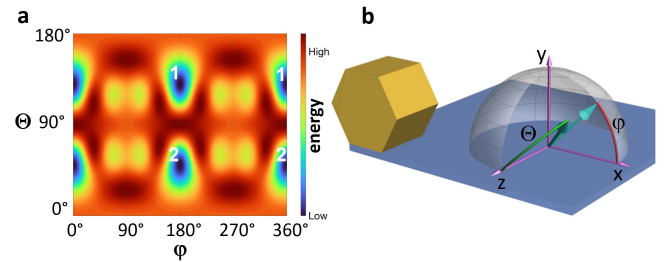


FIG. 5. **Néel vector orientation and free energy.** **a** Color scale representation of the dependence of the free energy on the Néel vector orientation. θ represents the polar angle with respect to the z -direction and φ the azimuthal angle of the Néel vector. **b** Corresponding coordinate system illustrating the orientation of the unit cell relative to the substrate.

By keeping the number of free parameters to a minimum, we are able to reproduce the experimentally observed tilting of the Néel vector away from the hexagonal c -axis by considering a single DMI term imposed by the hexagonal symmetry, resulting in a twelvefold degeneracy of the ground state Néel-vector orientations. The inclusion of an additional in-plane strain–induced DMI term partially lifts this degeneracy, resulting in four remaining energetically equivalent directions as shown in the energy map in Fig. 5. The calculated free-energy landscape exhibits four absolute minima (dark blue in the color map), corresponding to four equivalent ground-state orientations of the Néel vector. Among these, those labeled 1 are associated with a DMI induced weak magnetization parallel to the y -direction, whereas those labeled 2 correspond to an antiparallel orientation.

We further use symmetry considerations to model the relationship between the AHE and the Néel vector. As described in detail in the Supplementary Information, we expand the general resistivity tensor R_{ij} in terms of the magnetic variables and retain only the lowest order terms consistent with the point symmetry group of the nonmagnetic phase. Due to strong exchange coupling between sublattices, we note that the value of magnetization is negligibly small. However, the magnetization vector has the same symmetry as the Hall vector and can therefore be used to describe the field dependence of the resistivity. In our measurement geometry with the current applied along the x -direction, the AHE is therefore sensitive to the z -component of the Néel vector, n_z , and to the y -component, \hat{m}_y , of the unit vector $\hat{\mathbf{m}}$ parallel to magnetization :

$$\rho_{\text{AHE}} = \alpha_{\text{AHE}} Q_{\text{AM}} n_z + \beta_{\text{AHE}} \hat{m}_y(\mathbf{n}), \quad (1)$$

where Q_{AM} is the altermagnetic order parameter, α_{AHE} and β_{AHE} are phenomenological constants.

All four ground state orientations of the Néel vector shown in Fig. 5 are energetically degenerate and therefore occur with equal probability, resulting in an equal

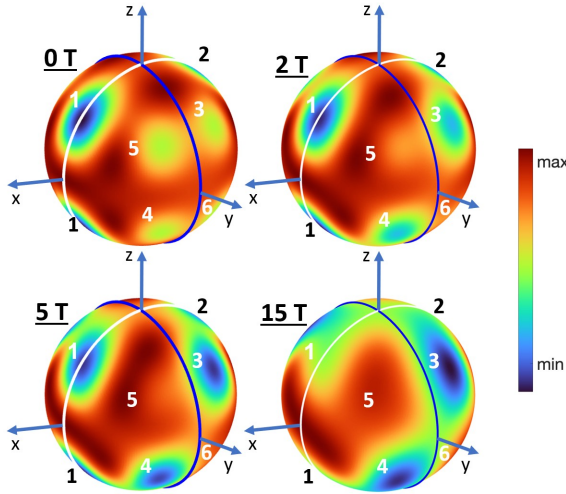


FIG. 6. **Field driven Néel vector orientation.** Energy maps associated with the Néel vector orientation projected on a sphere for different magnitudes of the magnetic field tilted by $\phi = 2^\circ$ from the x -direction towards the y -direction.

population of domains in zero magnetic field. Averaging over these domains naturally explains the absence of an AHE in the experimental data at zero field.

However, we experimentally observed an AHE when the magnetic field is tilted slightly out of the film plane (Fig. 2). Accordingly, in our simulations we consider the application of a magnetic field tilted by $\phi = 2^\circ$ from the x -axis (in-plane [1000]-direction) towards the y -axis. The corresponding energy landscapes, shown in Fig. 6 as a projection onto a sphere, illustrate how the energy minima evolve with increasing magnetic field.

A transition of the absolute energy minima from positions 1 and 2 at zero field to position 3 occurs at a magnetic field of $\simeq 5$ T. This field-induced reorientation of the Néel vector is therefore suggested as the source of the pronounced non-linearity and hysteresis observed experimentally in the Hall-effect within this field range.

Panel a of Fig. 7 displays the energy of all local minima that attain the lowest overall energy within any part of the experimentally accessed field range. Minima that are energetically equivalent in our geometry are assigned the same label in the inset showing the zero field energy map.

Using Eq.(1), we calculate the AHE associated with these energy minima. Panel b of Fig. 7 presents the AHE corresponding to the Néel vector orientations labeled 1-4. The contributions of both terms in Eq.(1) are found to be comparable in magnitude and are therefore shown separately in the Supplementary Information.

Next, we consider the field-dependent evolution of the Néel vector and the corresponding AHE in analogy to our experiments. We consider starting a magnetic field sweep from a large positive value. In this regime, the Néel vector orientation labeled 3 is lowest in energy (red line in panel a of Fig. 7), and the corresponding AHE (red

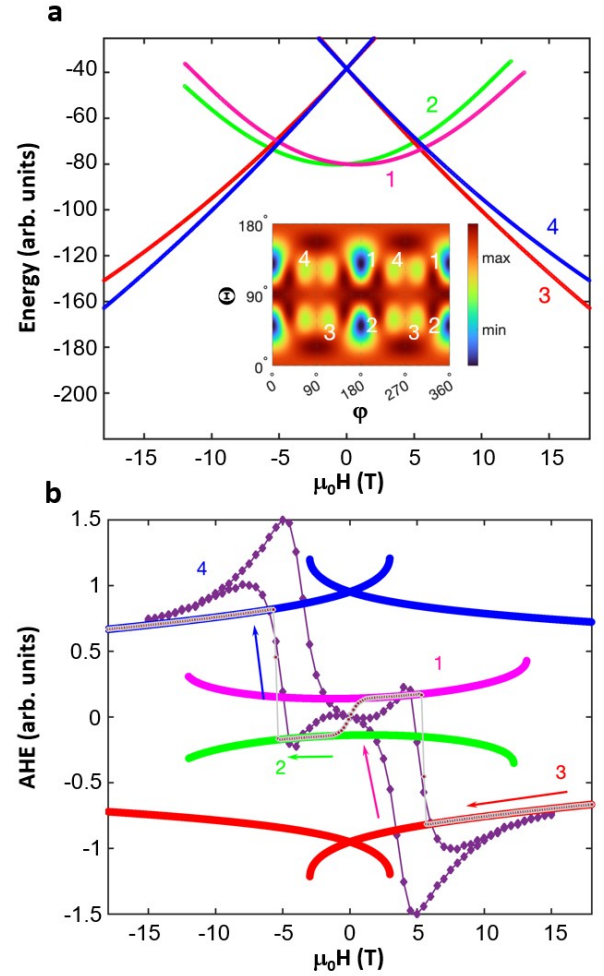


FIG. 7. **Field driven Néel vector orientation and AHE.** Panel a shows the energy associated with the Néel vector orientations labeled in the inset. Panel b shows the AHE corresponding to these orientations. By sweeping from positive to negative magnetic fields, the lowest energy orientation of the Néel vector changes from 3 to 1 to 2 to 4 corresponding to the AHE indicated by the gray data points. The violet data point show experimental results for comparison.

line in panel b) is negative, in agreement with the experimental data (violet data points). At $\simeq 5$ T, Néel vector configuration 1 becomes energetically favorable, resulting in a relatively small positive AHE (pink curve). This sign change again agrees with the experimental observations, which additionally exhibit hysteretic behavior, as expected for a multidomain state in which the growth of specific domains is associated with domain wall motion and pinning. Upon further decreasing the magnetic field to negative field values, configuration 2 becomes energetically favorable, leading to another sign change of the AHE (green curve). Finally, at $\simeq 5$ T, configuration 4 corresponds to the energy minimum, resulting in a relatively large positive AHE (blue curve).

Overall, the calculated AHE corresponding to the low-

est energy orientation of the Néel vector (gray curve in Fig. 7b) shows good qualitative agreement with the experimentally observed Hall-effect for magnetic fields tilted by 2° out of the sample plane from the [1000]-direction (pink data points in Fig. 7b). This agreement strongly supports the conclusion that the hysteretic nonlinearities observed experimentally in the Hall effect of $\text{Cr}_{0.75}\text{Mn}_{0.25}\text{Sb}(100)$ originate from an AHE enabled by altermagnetism.

In summary, partial substitution of Cr by Mn in epitaxial $\text{CrSb}(100)$ thin films modifies the magnetic easy direction, thereby engineering the symmetry that enables the occurrence of an anomalous Hall effect (AHE). Guided by Landau theory, we model the field driven orientation of the Néel vector and the associated AHE, achieving good qualitative agreement with the experimental observations. This allows us to reliably conclude that the pronounced hysteretic and nonlinear behavior observed in the magnetic field dependence of the Hall signal is indeed an AHE arising from the altermagnetic nature of $\text{Cr}_{0.75}\text{Mn}_{0.25}\text{Sb}$. Our experiments demonstrate the feasibility of tuning the electronic and magnetic properties of established altermagnets to meet the required symmetry for electrical read-out in spintronics applications. In particular, we have shown that CrSb , an altermagnet with exceptionally high ordering temperature and electrical conductivity, can be engineered to enable electrical read-out of the Néel vector orientation via measurements of the AHE.

EXPERIMENTAL METHODS

Sample preparation and characterization

Epitaxial $\text{Cr}_{1-x}\text{Mn}_x\text{Sb}(100)$ thin films with a thickness of 30 nm were deposited on $\text{GaAs}(110)$ substrates by DC magnetron sputtering from a single cathode using a composite target composed of elemental segments of the constituent materials Cr, Mn, and Sb, each occupying either 1/16 or 1/8 of the total target area. Varying fractions of the Cr segments were replaced with Mn to obtain different magnetic phases of $\text{Cr}_{1-x}\text{Mn}_x\text{Sb}$. The deposition parameters were identical to those used for thin films of the parent compound CrSb [12].

Crystallographic characterization of the samples, presented in the Supplementary Information, was carried out by X-ray diffraction using a Bruker D8 Discover four-circle diffractometer and by scanning transmission electron microscopy (STEM) using a FEI Titan TEM.

Magnetotransport measurements

Magnetotransport measurements (Figs. 2 and 4) in magnetic fields below 15 T were performed using an Oxford Instruments Cryostat equipped with a variable temperature inset, a superconducting magnet, and a rotatable sample stage. The measurements were conducted

with a Keithley 6220 precision current source supplying a probe current of 10 μA and a Keithley 2182A Nanovoltmeter operated in Delta mode, with averaging over 100 measurements. The AMR measurement in magnetic fields above 15 T (Fig. 1d) were carried out at the Dresden High Magnetic Field Laboratory using pulsed magnetic fields with a duration of 100 ms. Data were acquired at a sampling rate of 80 kHz using a numerical lock-in technique [22].

The samples were lithographically patterned into stripes and crosses aligned with the crystallographic directions of the thin films as indicated in Figs. 1, 2, and 3.

Magnetization measurements

Magnetization measurements (see Supplementary Information) were performed using a superconducting quantum interference device (SQUID) magnetometer (Quantum Design MPMS), equipped with a 5 T superconducting magnet.

Acknowledgements

We acknowledge funding by the Deutsche Forschungsgemeinschaft (DFG, German Research Foundation) - TRR 173 - 268565370 (projects A05, A11, A01, and B02).

Author contributions M.G.F., L.O., O.G. and M.J. wrote the paper, M.G.F. and L.O. prepared the samples. M.G.F., L.O., and M.J. performed all measurements, supported by T.K. and T.H. at the high field lab; O.G. simulated the AHE based on her theoretical model, T.D. and R.D.-B. provided the STEM images, M.K. and J.S contributed to the discussion of the results and provided input. M.J. coordinated the project.

Competing interests:

The authors declare no competing financial interests.

- [1] Šmejkal, L., González-Hernández, R., Jungwirth, T., and Sinova, J. Crystal time-reversal symmetry breaking and spontaneous Hall effect in collinear antiferromagnets. *Sci. Adv.* **6**, eaaz8809 (2020).
- [2] Hayami, S., Yanagi, Y., Kusunose, H. Momentum-Dependent Spin Splitting by Collinear Antiferromagnetic Ordering. *J. Phys. Soc. Jpn.* **88**, 123702 (2019).
- [3] Mazin, I. I., Koepernik, K., Johannes, M. D. and Šmejkal, L. Prediction of unconventional magnetism in doped FeSb_2 . *Prod. Natl. Acad. Sci. U. S. A.* **118**, e2108924118 (2021).
- [4] Šmejkal, L., Sinova, J., Jungwirth, T. Beyond Conventional Ferromagnetism and Antiferromagnetism: A Phase with Nonrelativistic Spin and Crystal Rotation Symmetry. *Phys. Rev. X* **12**, 031042 (2022).
- [5] Šmejkal, L., Sinova, J., Jungwirth, T. Emerging Research Landscape of Altermagnetism. *Phys. Rev. X* **12**, 040501 (2022).
- [6] Dzyaloshinsky, I. A thermodynamic theory of weak fer-

romagnetism of antiferromagnets. *J. Phys. Chem. Solids* **4**, 241 (1958).

[7] Gonzalez Betancourt, R. D. G., Spontaneous anomalous Hall effect arising from an unconventional compensated magnetic phase in a semiconductor. *Phys. Rev. Lett.* **130**, 036702 (2023).

[8] Kluczyk, K. P. et al. Coexistence of anomalous Hall effect and weak magnetization in a nominally collinear antiferromagnet MnTe. *Phys. Rev. B* **155** 201 (2024).

[9] Krempaský, J. et al. Altermagnetic lifting of Kramers spin degeneracy. *Nature* **626**, 517 (2024).

[10] Lee, S. et al. Broken Kramers Degeneracy in Altermagnetic MnTe. *Phys. Rev. Lett.* **132**, 036702 (2024).

[11] Osumi, T. et al. Observation of a giant band splitting in altermagnetic MnTe. *Phys. Rev. B* **109**, 115102 (2024).

[12] Reimers, S. et al. Direct observation of altermagnetic band splitting in CrSb thin films. *Nat. Commun.* **15**, 2116 (2024).

[13] Ding, J. et al. Large Band Splitting in g-Wave Altermagnet CrSb. *Phys. Rev. Lett.* **133** 206401 (2024).

[14] Zhou, Z. et al. Manipulation of the altermagnetic order on CrSb via crystal symmetry. *Nature* **638**, 645 (2025).

[15] Park, I.J., Kwon, S., and Lake, R.K., Effects of filling, strain, and electric field on the Néel vector in antiferromagnetic CrSb. *Phys. Rev. B* **102**, 224426 (2020).

[16] Takei, W.J., Cox, D.E., Shirane, G, Magnetic Structures in the MnSb-CrSb System. *Phys. Rev.* **129**, 2008 (1963).

[17] Reimers, W., Hellner, E., Treutmann, W., Heger, G., Magnetic phase diagram of the system $Mn_{1-x}Cr_xSb$. *J. Phys. C: Solid State Phys.* **15**, 3597 (1982).

[18] Kino, H., Ikuse, K., Dam, H.-C., Hamaguchi, S. Characterization of descriptors in machine learning for data-based sputtering yield prediction. *Phys. Plasmas* **28**, 013504 (2021). <http://www.camt.eng.osaka-u.ac.jp/hamaguchi/SY/>

[19] Snow, A. I. Neutron Diffraction Invesitgation of the Atomic Moment Orientation in the Antiferromagnetic Compound CrSb. *Phys. Rev.* **85**, 365 (1952).

[20] Machado, F.L.A., Ribeiro, P.R.T., Holanda, J., Rodríguez-Suárez, R.L., Azevedo, A. and Rezende, S.M. *Phys. Rev. B* **95**, 104418 (2017).

[21] Gomonay, O. et al. Structure, control, and dynamics of altermagnetic textures. *npj Spintronics* **2**, 35 (2024).

[22] Bodnar, S. et al. Magnetoresistance Effects in the Metallic Antiferromagnet Mn₂Au. *Phys. Rev. Appl.* **14**, 014004 (2020).